

# Exact resolution function for double-disk chopper neutron time-of-flight spectrometers : Application to reflectivity

Didier Lairez,<sup>1,2,\*</sup> Alexis Chennevière,<sup>1</sup> and Frédéric Ott<sup>1</sup>

<sup>1</sup>Laboratoire Léon Brillouin, CEA-CNRS-Université Paris-Saclay, 91191 Gif-sur-Yvette, France

<sup>2</sup>Laboratoire des solides irradiés, CEA-École polytechnique-CNRS-Institut Polytechnique de Paris, 91128 Palaiseau, France

(Dated: September 4, 2022)

The exact resolution function in transfer vector for the reflectometer HERMÈS at Laboratoire Léon Brillouin is calculated as an example of neutron time-of-flight spectrometer with double-disk chopper. Calculation accounts for wavelength distribution of the incident beam, tilt of the chopper axis, collimation and gravity, without approximation of gaussian distributions or independence of these different contributions. Numerical implementation is provided that matches the sections of the paper. We show that data fitting using this exact resolution function allows us to reach much better results than its usual approximation by a gaussian profile.

## I. INTRODUCTION

It is quite common for physical measurements to attempt to reach the limit of a given technique. In many cases, this amounts to measure a quantity with an accuracy better than the resolution of the apparatus. Said like that, it seems impossible. For instance, how to discriminate the position of two peaks which are closer from each other than their width? It is possible if we expect a given shape for each peak, do the convolution of expectation with the resolution function of the apparatus and compare the result with the measurement (this is commonly called “data fitting”). Another example: neutron specular reflectivity allows us to get structural informations on thin layers at an interface i.e. layers thicknesses and densities (for an introduction to reflectivity see for instance [1]). The latter are determined relative to the scattering length density difference  $\Delta\rho$  between the two infinite media separated by the interface and consequently from the value of the critical transfer vector  $q_c$  below which total reflexion occurs; e.g. for the air/silicon interface  $q_c = 0.0102 \text{ \AA}^{-1}$  yields to  $\Delta\rho = q_c^2/16\pi = 2.07 \times 10^{10} \text{ cm}^{-2}$ , which is the correct result. A shift of 3% for  $q_c = 1.03 \times 0.0102 \text{ \AA}^{-1}$  gives  $\Delta\rho = 2.20 \times 10^{10} \text{ cm}^{-2}$ , which is not acceptable for many users of reflectometers. But 3% is the order of magnitude of the resolution. This barrier can be bypass if we know that the reflectivity curve should obey to a given function. To reach these limits, the calculation of the resolution function has to be as accurate as possible. In particular the approximation that all random variables that contribute to the resolution have a gaussian probability density is likely not satisfactory [2] especially in case the resolution is relaxed to gain flux. This approximation, which was legitimate when the means of calculation were insufficient, is no longer justified.

Neutrons diffraction, scattering or reflectivity measurements take a “picture” of a sample in the reciprocal space

for which the conjugate variable of distance is the transfer vector  $q$  that is practically proportional to the ratio of the incident angle  $\theta$  to the wavelength  $\lambda$ . Basically the resolution  $\sigma_q$  is such as  $(\sigma_q/q)^2 \simeq (\sigma_\theta/\theta)^2 + (\sigma_\lambda/\lambda)^2$  (where  $\sigma$  holds for standard deviations). On the other hand, if we do not account for the transfer function of the sample, the signal is proportional to the incident neutron-flux i.e. to the product  $\sigma_\theta\sigma_\lambda$ . Thus for a given flux, the minimum for  $\sigma_q/q$  is obtained for  $\sigma_\theta/\theta = \sigma_\lambda/\lambda$ . Time-of-flight techniques do the work at constant  $\theta$  (thus constant  $\sigma_\theta/\theta$ ) as a function of  $\lambda$ . If we require a constant flux, since  $\sigma_\theta/\theta$  is constant,  $\sigma_\lambda/\lambda$  should also be constant. This is achieved with double-disk choppers [3] and this argument is the major reason of their wide spread. The counterpart is a broad resolution  $\sigma_\lambda$  at large wavelength, precisely in the region where a good accuracy is often needed (edge of the total reflexion plateau). Hence the interest of making an exact calculation of the resolution function.

In this paper we present the calculation of the overall and exact resolution function for the reflectometer HERMÈS at Laboratoire Léon Brillouin. In spite its current neutron source is continuous (Orphée reactor), this spectrometer is based on the time-of-flight principle that is to become generalized with the increase of pulsed neutron sources, it is equipped with a double-disk chopper that is now a standard. So, the step-by-step calculation developed here has a broad scope. For the most part, the different contributions to the final resolution have already been mentioned separately in the literature: wavelength distribution of the incident beam, tilt of the chopper axis, collimation and gravity. But, here they are all presented in a uniform and comprehensive manner that makes the procedure likely easier to implement and adapt in each specific case and even to extend for other techniques such as small-angle scattering or diffraction. We write analytically the whole resolution function that accounts for all these contributions without any approximation of gaussian distributions or independence of the different contributions. We show that data fitting using this exact resolution function allows us to reach much more accurate results than its usual approximation by a gaussian profile. Also, a python code that implements these cal-

\*Electronic address: lairez@cea.fr

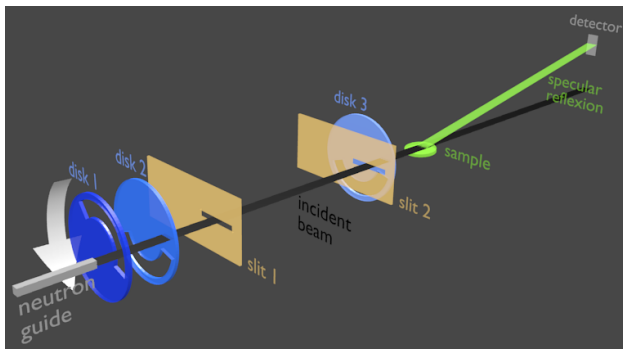


FIG. 1: Schematic diagram of HERMÈS reflectometer.

culations is provided.

## II. BRIEF DESCRIPTION OF THE REFLECTOMETER

In Fig.II, a schematic diagram of the reflectometer is shown. Neutron-pulses are produced by a three-disk chopper of same characteristics from Airbus company (numbered 1, 2 and 3 with respect to neutrons trajectory). In the standard configuration these disks rotate in the same direction at a pulsation  $\omega$  around the same axis. Also, they have a fixed angular aperture of same width  $\varphi_a = 165^\circ$  allowing neutrons to pass. Disk 2 and 3 are in a fixed position 2m from each other, whereas disk 1 can be placed at three different distances from disk 2 (0.1, 0.35 and 1 m, respectively). Essentially, disk 1 and 2 control the wavelength resolution whereas disk 3 is mainly devoted to avoid the time-overlap of the slowest neutrons of a given pulse with the fastest of the next one.

The collimator is basically made of two horizontal slits of half-width  $r_1$  and  $r_2$  (numbered 1 and 2 with respect to neutrons trajectory) located between disk 2 and 3, at the same height and spaced by  $d_c = 1.8$  m. The width of the slits are tuned so that the angular resolution remains consistent with the wavelength resolution resulting from the disk chopper parameters. In the following, we will consider three different typical configurations summarized in Table I that correspond to high (HR), medium (MR) and low resolution (LR), respectively.

Specular reflexion at the desired angle  $\theta_0$  is obtained by rotation of the sample. In case a non-horizontal beam is needed (e.g. for the study of horizontal liquid surfaces), two plane mirrors are placed in the collimator to deviate the beam. These mirrors have no incidence on the resolution and will be ignored in the following. Specular reflexion is measured in a vertical plane at angle  $2\theta_0$  with a detector whose wide aperture allows all reflected neutrons to be captured whatever their trajectory.

TABLE I: Typical configurations corresponding to high (HR), medium (MR) and low resolution (LR).  $x(1)$ ,  $x(2)$ ,  $x(3)$  and  $x(4)$  are the positions of disk 1, 2, 3 and of the detector, respectively.  $2r_1$  and  $2r_2$  are the widths of the first and second slit of collimator at fixed distance  $d_c = 1800$  mm apart. All lengths are in mm

	HR	MthatR	LR
$x(4) - x(3)$		2375	
$x(3) - x(2)$		2000	
$x(2) - x(1)$	100	350	1000
$2r_1$	1	2	4.6
$2r_2$	1	1	1

## III. WAVELENGTH RESOLUTION

The wavelength resolution results basically from the incident beam distribution and from the transfer function of the chopper. The latter is mainly controlled by the phases of the first two-disks (hence our title), but in a general way the third also should be accounted for at long wavelength. In this section we examine these different points and present the way to calibrate the phases in question.

### A. Resolution of a double-disk chopper

We first consider a chopper made only of the first two disks. Let us denote  $x(i)$  the positions (as in Table I),  $\varphi_o(i)$  the phase for disk opening and  $\varphi_c(i)$  the phase for disk closure. By convention, we denote the actual phase as  $\omega t - \varphi$ , so that  $\varphi > 0$  states for a delay. The measurement consists in recording the number of neutron arrivals at time  $t_0$  over a timebase that is periodically restarted (triggered) at each revolution of the chopper, so that to  $t_0$  corresponds a phase of arrival  $\varphi(4) = \omega t_0$ . Fig.2 shows the corresponding time-of-flight diagram using  $\omega t$  as abscissa. From the de Broglie's equation, in this diagram the kinematics curve of a neutron of wavelength  $\lambda$  and velocity  $v$  is a straight-line with the reverse slope

$$\frac{\omega}{v} = \frac{\omega}{h/m} \times \lambda \quad (1)$$

with  $h$  the Planck's constant,  $m$  the mass of neutron and  $h/m = 3956 \text{ Å m/s}$ .

Simple geometrical considerations (see Fig.2) show that neutrons with phase of arrival  $\varphi(4) = \omega t_0$  have a velocity between  $v_1$  and  $v_2$  such as

$$\frac{\omega}{v_1} = \frac{\varphi(4) - \varphi_c(1)}{x(4) - x(1)} \quad \text{and} \quad \frac{\omega}{v_2} = \frac{\varphi(4) - \varphi_o(2)}{x(4) - x(2)} \quad (2)$$

which are symbolized by the two red lines in Fig.2. The bisector of these two lines (red dashed line) has a reverse

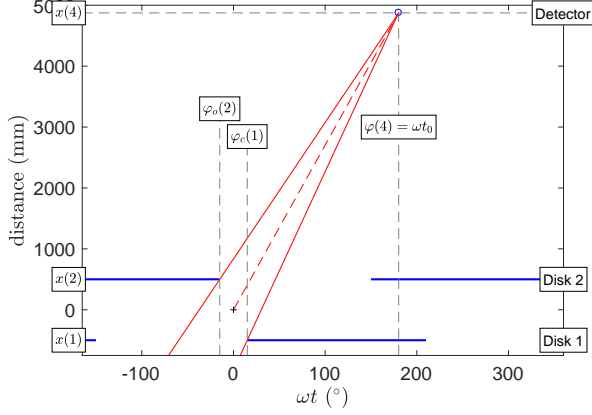


FIG. 2: Double chopper: flight distance vs. phase  $\omega t$ . In blue the closed sector of disks. Neutrons that reach the detector at phase  $\varphi(4) = \omega t_0$  have a kinematics that lies between the two red lines which slopes are given by Eq.2. The dashed line in red is the bisector and states for the nominal wavelength.

slope that writes

$$\frac{\omega}{v_0} = \frac{\varphi(4) - \left(\frac{\varphi_c(1) + \varphi_o(2)}{2}\right)}{x(4) - \left(\frac{x(1) + x(2)}{2}\right)} \quad (3)$$

The choice for the origine of phase just between opening of disk 2 and closure of disk 1 and the origine of distance between disk 1 and 2 is quite natural. With these coordinates one has

$$\frac{\omega}{v_0} = \frac{\varphi(4)}{x(4)} \quad (4)$$

that defines for the double-disk chopper the nominal wavelength that is simply proportional to the time-of-flight.

Let us denote

$$\epsilon = \frac{\varphi_o(2) - \varphi_c(1)}{2} \quad \text{and} \quad h = \frac{x(2) - x(1)}{2} \quad (5)$$

Then Eq.2 rewrites

$$\frac{\omega}{v_1} = \frac{\varphi(4) - \epsilon}{x(4) + h} \quad \text{and} \quad \frac{\omega}{v_2} = \frac{\varphi(4) - \epsilon}{x(4) - h} \quad (6)$$

To these boundaries correspond the wavelengths  $\lambda_1$  and  $\lambda_2$  that allow us to define the half range of transmitted wavelength  $\Delta\lambda$  and the median wavelength  $\lambda_0$  as :

$$\Delta\lambda = \frac{\lambda_2 - \lambda_1}{2}; \quad \lambda_0 = \frac{\lambda_2 + \lambda_1}{2} \quad (7)$$

From Eq.6, one gets :

$$\Delta\lambda = \frac{h/m}{\omega} \times \frac{\varphi(4)h + x(4)\epsilon}{x(4)^2 - h^2} \quad (8)$$

and

$$\lambda_0 = \frac{h/m}{\omega} \times \frac{\varphi(4)x(4) + \epsilon h}{x(4)^2 - h^2} \quad (9)$$

Note that in the general case ( $\epsilon \neq 0$ ) the median  $\lambda_0$  is not simply proportional to the time-of-flight. The relative resolution of the chopper is

$$\frac{\Delta\lambda}{\lambda_0} = \frac{\varphi(4)h + x(4)\epsilon}{\varphi(4)x(4) + \epsilon h} \quad (10)$$

In the case  $\epsilon = 0$ , one obtains :

$$\frac{\Delta\lambda}{\lambda_0} = \frac{h}{x(4)} \quad (11)$$

so that the relative resolution of the chopper is constant whatever the time of arrival  $t_0$ . This is the main reason for using double-disk chopper as it allows us to optimize the resolution with respect to neutron-flux [3]. From Table I, the three standard configurations correspond to  $\Delta\lambda/\lambda_0 = 1, 4$  and 10%, respectively.

### B. Three-disk chopper and time-of-flight channel

The general case of a three-disk chopper is a bit more complicated because for long time-of-flight the third disk comes into play. This implies a modification of Eq.2. In standard configurations  $\varphi_c(1) \simeq \varphi_o(2) \simeq \varphi_o(3)$ , so that the velocity  $v_1$  of fastest neutrons that reach the detector at phase  $\varphi(4)$  is limited either by the closure of disk 1 or disk 3 (see Fig.3) and the velocity  $v_2$  of slowest neutrons is limited by the opening of disk 2 or disk 3. This can be formalized in the general case as :

$$\frac{\omega}{v_1} = \max_{i \in \{1,2,3\}} \frac{\varphi(4) - \varphi_c(i)}{x(4) - x(i)}; \quad \frac{\omega}{v_2} = \min_{i \in \{1,2,3\}} \frac{\varphi(4) - \varphi_o(i)}{x(4) - x(i)} \quad (12)$$

The last point is that neutron counters record the number of neutron-arrivals in the time interval between  $t_0 - \Delta t$  and  $t_0 + \Delta t$  referred to as a “time-of-flight channel”. The phases for the opening and closure of this channel are  $\varphi_o(4) = \omega(t_0 - \Delta t)$  and  $\varphi_c(4) = \omega(t_0 + \Delta t)$  and Eq.12 rewrites :

$$\frac{\omega}{v_1} = \max_{i \in \{1,2,3\}} \frac{\varphi_o(4) - \varphi_c(i)}{x(4) - x(i)}; \quad \frac{\omega}{v_2} = \min_{i \in \{1,2,3\}} \frac{\varphi_c(4) - \varphi_o(i)}{x(4) - x(i)} \quad (13)$$

In Fig.4, the relative half range of transmitted wavelengths calculated from these two boundaries is plotted for 256 time-of-flight channels covering  $360^\circ$  of a chopper revolution for the three typical configurations of Table I. The curves show a plateau corresponding to the “double-disk” chopper regime described by Eq.11. At large wavelength, the decreasing of the resolution is due to the third disk that comes into play, whereas at short wavelength departure from the plateau is due to the channel width.

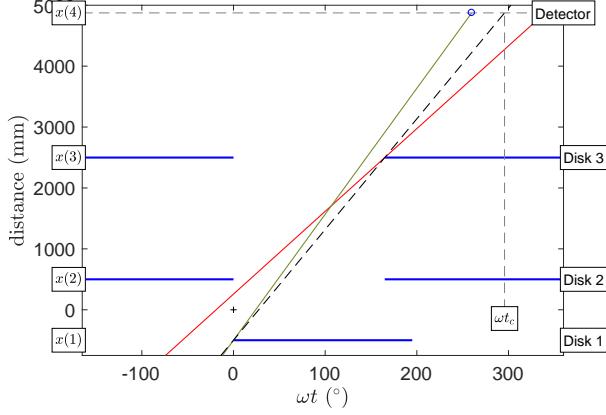


FIG. 3: Three-disk chopper: compared to Fig.2, the 3rd disk comes into play for long time-of-flight. The dashed line in black with slope  $(x(3) - x(1))/(\varphi_c(3) - \varphi_c(1)) = (x(4) - x(1))/(\omega t_c - \varphi_c(1))$  delimits two regimes for the velocity  $v_1$  of fastest neutrons that is limited either by the closure of disk 1 (red), or by the one of disk 3 (green). The same occurs for slow neutrons of velocity  $v_2$  (case not shown).

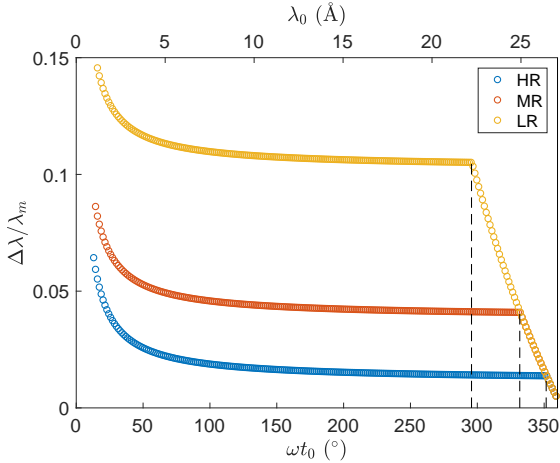


FIG. 4: Relative half range of transmitted wavelengths  $\Delta\lambda/\lambda_0$  versus phase  $\omega t_0$  for 256 time-of-flight channels covering  $360^\circ$  of data-acquisition for the three standard configurations of Table I with  $\varphi_c(1) = \varphi_o(2) = \varphi_o(3)$ . The top x-axis is the median wavelength  $\lambda_0$  for  $\omega = 30$  Hz. The dashed lines mark the separation  $\omega t_c$  of the two regimes delimited by the dashed line in Fig.3.

### C. Phase calibration and tilt of the chopper axis

The time resolved neutron counting is triggered at each revolution by the chopper electronics. On this subject, the only unknown parameter is the phase shift  $\phi_{\text{trig}}$  of this trigger with respect to the physical origin of phases. This point is resolved by measuring the transmission of a crystalline material (e.g. a graphite crystal) that displays

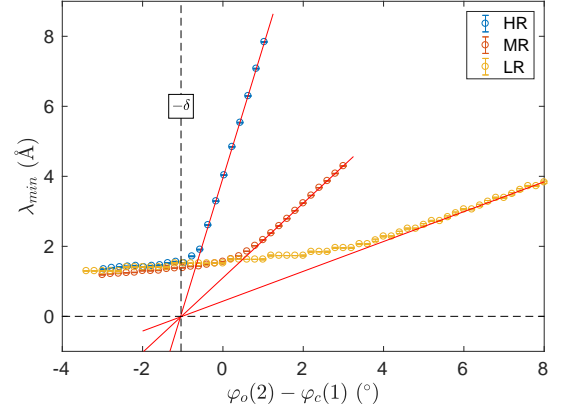


FIG. 5: Minimum wavelength  $\lambda_{\min}$  as a function of  $\varphi_o(2) - \varphi_c(1)$ , measured for the three different configurations of Table I; at  $\omega = 30$  Hz. Extrapolation to  $\lambda_{\min} = 0$  gives the angle  $\delta = 1^\circ$  that should be added to the phase of disk 2.

a characteristic attenuation at wavelength  $\lambda^*$  [4]. No matter the value of  $\lambda^*$ , the corresponding time-of-flight  $t^*$  is constant and the related phase writes  $\phi^* = \omega t^* + \phi_{\text{trig}}$ . Measuring  $\phi^*$  as a function of  $\omega$  and extrapolating to  $\omega = 0$  gives  $\phi_{\text{trig}}$ .

Taking the rotation of disk 1 as a reference, the phase shift of disk 2 and 3 are chosen by the experimentalist and kept constant by the electronics with a control loop feedback, which ensures that no variation or drift occurs during measurements. However, possible differences between phases setpoints and their actual values have to be measured. Also, a vertical tilt or misalignment of the centers of the three disks with the spectrometer axis affects the kinematics line of neutrons allowed to pass through the chopper in the same manner as a phase difference. Hence the need of disk-phase calibration.

The phase of disk 2 affects the short-wavelength cut-off ( $\lambda_1$ ) and the chopper resolution in the first regime of Fig.4, whereas the phase of disk 3 affects the large-wavelength cutoff ( $\lambda_2$ ) in the second regime and the time-of-flight channel at which this regime begins. Let us first consider the former. From Fig.2, one can see that the fastest neutrons passing through the chopper are such that  $\omega/(h/m) \times \lambda_{\min} = \omega/v_{\max} = \epsilon/h$ . In Fig.5, the measured  $\lambda_{\min}$  is plotted as a function of  $\varphi_o(2) - \varphi_c(1) = 2\epsilon$ , the linear behavior of the cut-off does not pass through the origin: a constant  $\delta$  (here equal to  $1^\circ$  for the three configurations) should be added to  $\varphi_o(2) - \varphi_c(1)$  in order to obtain the correct value for  $\lambda_{\min}$ . In practice, the phase of disk 2 in Eq.13 has to be increased by  $\delta$ . Note that the method here reported to measure  $\varphi_o(2)$  is equivalent to measuring the intensity of a monochromatic beam as a function of the phase  $\varphi_o(2) - \varphi_c(1)$  [5], but is probably simpler to perform routinely because no monochromator is needed.

In the same way, the large-wavelength cut-off of the

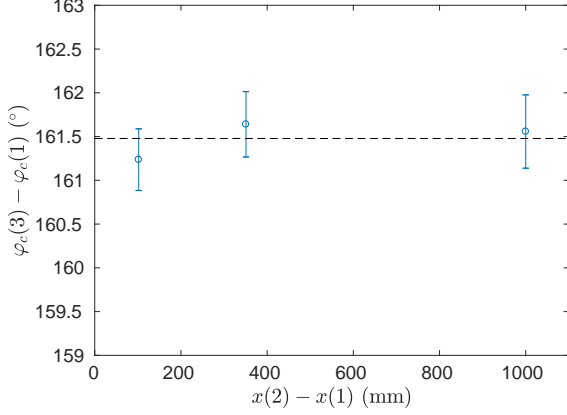


FIG. 6: Value of the phase  $\varphi_c(3)$  deduced from Eq.14 and the measurement of the phase  $\omega t_c$  of the large wavelength cut-off for a setpoint  $\varphi_c(3) = 165^\circ$ . The difference with this setpoint gives  $\eta = -3.5^\circ$  that should be added to the phase of disk 3.

chopper transmission allows us to determine the actual phase of disk 3. The phase  $\omega t_c$  of the cut-off (see Fig.3), is such as :

$$\frac{\omega t_c - \varphi_c(1)}{(x(4) - x(1))/(x(3) - x(1))} = \varphi_c(3) \quad (14)$$

From the measurement of  $\omega t_c$  the actual value of  $\varphi_c(3)$  can be deduced (Fig.6). We found that a constant value  $\eta = -3.5^\circ$  has to be added to the phase of disk 3.

#### D. Incident beam and detector efficiency

For a white beam of uniform distribution, the probability density  $D(\lambda)$  of wavelength for neutrons passing through the chopper with phase of arrival  $\omega t_0$  is a rectangular function that writes:

$$D(\lambda) = \begin{cases} 0 & , \text{ if } \lambda \notin [\lambda_1, \lambda_2] \\ 1/(\lambda_2 - \lambda_1) & , \text{ if } \lambda \in [\lambda_1, \lambda_2] \end{cases} \quad (15)$$

where  $\lambda_1$  and  $\lambda_2$  are the wavelength boundaries of the time-of-flight channel given by Eq.13.

Thermalized neutrons have a Maxwell-Boltzmann distribution of velocity that is altered by neutron guides. Also, detectors efficiency exponentially decays with wavelength. Let us denote  $H_B(\lambda)$  the effective wavelength distribution that is the product of the actual distribution by the detector efficiency.  $H_B(\lambda)$  is the only observable variable. For a given time-of-flight channel, chopping a neutron beam amounts to applying the rectangular function  $D(\lambda)$  of Eq.15 to  $H_B(\lambda)$  [2] (see Fig.7). The probability density of wavelength for neutrons recorded in this channel is

$$H(\lambda) = H_B(\lambda)D(\lambda) \quad (16)$$

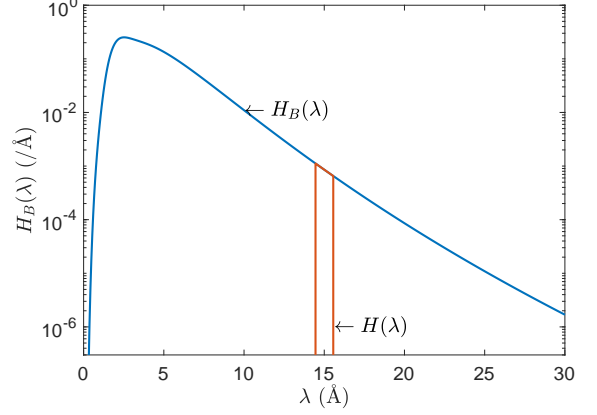


FIG. 7: Effective wavelength distribution  $H_B(\lambda)$  (blue) of the incident beam provided by the reactor Orphée on the guide G6-2 and wavelength distributions  $H(\lambda)$  (not normalized) for one time-of-flight channels centered on  $\lambda_0 = 15 \text{ \AA}$  (red) with  $\Delta\lambda/\lambda_0 = 0.04$ .

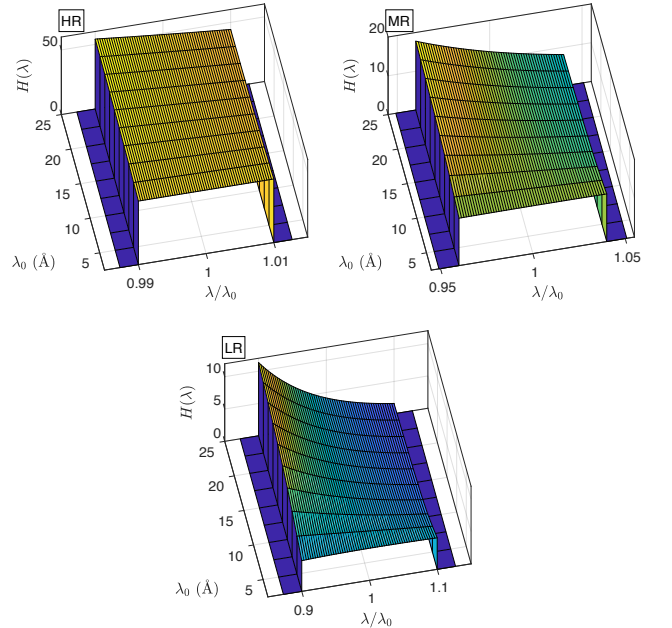


FIG. 8: Wavelength distributions  $H(\lambda)$  (Eq.16) vs.  $\lambda/\lambda_0$  (x-axis) and vs. time-of-flight channel centered on the median wavelength  $\lambda_0$  (y-axis). Calculated for the three configurations of Table I with  $\Delta t = 0$ ,  $\epsilon = 0$ .

$H_B(\lambda)$  can be measured using a single-disk chopper with a small  $\Delta\lambda$  (i.e. much smaller than the three-disk chopper) independent of the time-of-flight channel. For further calculations,  $H_B(\lambda)$  can then be properly parametrized using an *ad hoc* function. In Fig.8, the wavelength distribution  $H$  is plotted for the different time-of-flight channels and for the three configurations

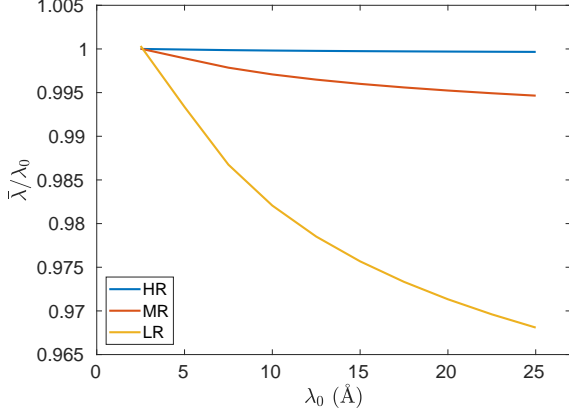


FIG. 9: Ratio of the mean wavelength  $\bar{\lambda}$  to the median wavelength  $\lambda_0$  vs.  $\lambda_0$  for the three configurations of Table I.

of Table I. The strong asymmetry of  $H(\lambda)$  results in an mean wavelength  $\bar{\lambda} = \int \lambda H(\lambda) d\lambda$  significantly different from the median  $\lambda_0$ . We plotted in Fig.9 the ratio  $\bar{\lambda}/\lambda_0$  as a function of the median  $\lambda_0$  for the three different chopper configurations of Table I. The wider the resolution, the more  $\bar{\lambda}$  deviates from  $\lambda_0$ .

#### IV. ANGULAR RESOLUTION

In this section, we focus on beam collimation and gravity, which both contribute to the final distribution of incidence angle of neutrons on the sample.

##### A. Beam divergence

Let us consider the divergence in the vertical plane of a neutron-beam collimated with two horizontal slits of half-width  $r_1$  and  $r_2$ , respectively, spaced by  $d_c$ . The distribution function of the angle  $\alpha$  of neutron trajectory results from the convolution of two rectangular functions centered on 0 and half-width  $r_1/d_c$  and  $r_2/d_c$ , respectively. This is a trapezoidal function that writes for  $r_1 > r_2$ :

$$P(\alpha) = \begin{cases} \frac{d_c}{2r_1} & \text{for } |\alpha| < \alpha_1 \\ \frac{d_c}{2r_1} \left( 1 - \frac{d_c}{2r_2} (|\alpha| - \alpha_1) \right) & \text{for } \alpha_1 < |\alpha| < \alpha_2 \\ 0 & \text{for } \alpha_2 < |\alpha| \end{cases}$$

$$\text{with } \alpha_1 = \frac{r_1 - r_2}{d_c} \text{ and } \alpha_2 = \frac{r_1 + r_2}{d_c} \quad (17)$$

As convolution is commutative, the two rectangular functions are fully interchangeable as far as only the beam divergence is concerned. So that, in case  $r_1 < r_2$

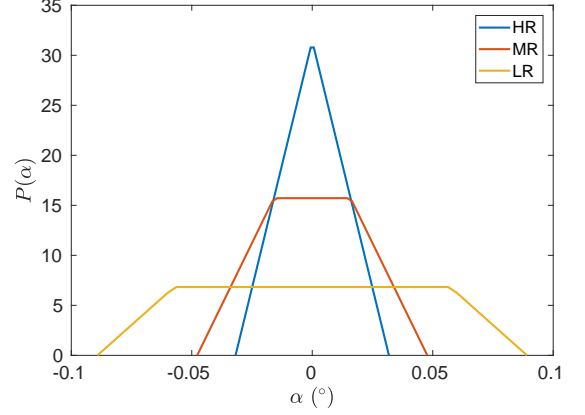


FIG. 10: Typical angular distribution  $P(\alpha)$  due to beam divergence for the three standard collimations of Table I.

their values can be exchanged in order Eq.17 to be applied. However for some reasons related to the beam size (the “footprint”  $2r_2 \sin(\theta)$  has to be smaller than the sample and also  $r_2$  restrains the accuracy of the alignment of the sample),  $r_1 > r_2$  is preferred and  $r_2$  is kept constant. In Fig.10 typical curves for  $P(\alpha)$  are plotted for standard collimations of Table I.

##### B. Deviation due to gravity

Due to gravity, neutrons deviate from a straight line and horizontal trajectory. This deflection increases with the time-of-flight (i.e. with the wavelength) and must be taken into account for specular reflectivity measured in the vertical plane [6]. Let us assume that the detector and the collimator slits are properly aligned to the neutron guide using a criterion of maximum neutron flux measured by integrating over the whole wavelength-distribution. As neutrons of short wavelength are majority (see Fig.7) and neglecting their deviation due to gravity, the line joining the two slits of the collimator is almost horizontal and the slits are at the same height. The apex of parabolic trajectories of all neutrons is thus at the middle between the two slits of the collimator. Let us denote  $v_x = \lambda/(h/m)$  and  $v_z$  the horizontal and vertical components of neutrons velocity, respectively. At the apex,  $v_z = 0$ . At any point beyond the apex  $v_z < 0$  and the deflection angle is  $\tan^{-1}(v_z/v_x) \simeq v_z/v_x$ . If  $d_1$  is the flight distance from the middle of the collimator to the sample, the time-of-flight is  $d_1/v_x$ , thus  $v_z = -gd_1/v_x$ , with  $g$  the gravitational acceleration. The deviation angle (which is always negative) on the sample is:

$$\gamma = \frac{-gd_1}{v_x^2} = -(c\lambda)^2 \quad \text{with} \quad c = \frac{(gd_1)^{1/2}}{h/m} \quad (18)$$

The distribution  $J(\gamma)$  of the deviation is related to the distribution of wavelength  $H(\lambda)$  via the general relation

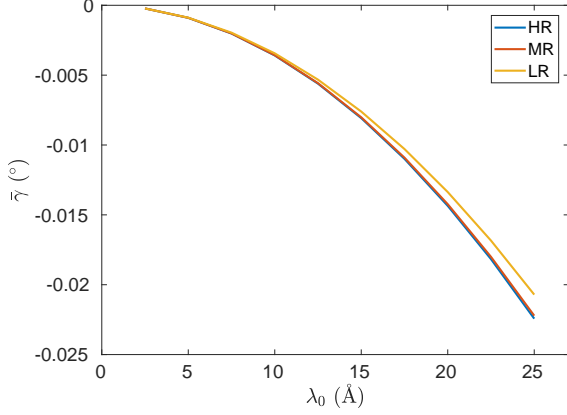


FIG. 11: Mean deviation  $\bar{\gamma}$  of neutrons due to gravity (for  $d_1 = 1$  m) vs.  $\lambda_0$  for the three configurations of Table I.

$J(\gamma) = H(\lambda) \times |d\lambda/d\gamma|$ , with  $\lambda = (-\gamma)^{1/2}/c$  (the inverse relation of Eq.18). One obtains:

$$J(\gamma) = \frac{1}{2c(-\gamma)^{1/2}} H((-\gamma)^{1/2}/c) \quad (19)$$

Basically,  $J(\gamma)$  has a shape comparable to  $H(\lambda)$  (i.e. a rectangular function applied to the wavelength distribution of the incident beam). Let us denote  $[\gamma_1, \gamma_2]$  the support interval of  $J(\gamma)$  and  $\Delta\gamma = (\gamma_2 - \gamma_1)/2$ . From Eq.18, one obtains  $\Delta\gamma = 2(c\lambda_0)^2 \times (\Delta\lambda/\lambda_0)$ . The quantity  $c$  is typically of the order of  $8 \times 10^{-4} \text{ \AA}^{-1}$  for  $d_1 = 1$  m, thus in a standard configuration  $\Delta\gamma$  is small compared to the beam divergence (support of  $P(\alpha)$ ). However, in case the relative angle resolution is very small compared to the wavelength resolution (*e.g.* binning of tof-channels to increase statistics [7], narrow collimation due to small size of the sample...) gravity should affect the width of the angular resolution. In any case, the main effect of gravity is due to the mean value  $\bar{\gamma} = \int \gamma J(\gamma) d\gamma$  that is non-zero and depends on the time-of-flight channel (i.e. on  $\lambda_0$ ). In Fig.11, the mean deviation  $\bar{\gamma}$  is plotted as a function of  $\lambda_0$ .

### C. Distribution of incidence angle

Let us denote  $\theta_0$  the nominal angle (i.e. the angle calculated from the inclination of the sample) of the neutron beam with respect to the interface under study. This angle is negative in case neutrons come from below the interface and positive if they come from over (this sign is imposed by gravity). The actual incidence angle  $\theta$  of neutrons on the sample is

$$\theta = \theta_0 + \alpha - \gamma \quad (20)$$

The distribution for  $\theta$  is thus given by

$$G(\theta) = \int P(\theta - \theta_0 + \gamma) J(\gamma) d\gamma \quad (21)$$

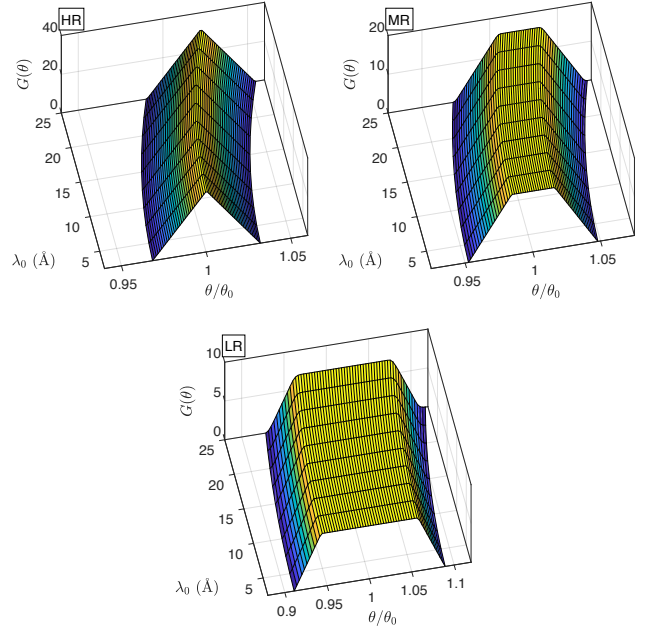


FIG. 12: Angular resolution  $G(\theta)$  vs.  $\theta/\theta_0$  (x-axis, where  $\theta_0 = 1^\circ$  is the nominal angle) and vs. time-of-flight channel centered on the median wavelength  $\lambda_0$  (y-axis), for the three configurations of Table I.

As  $J(\gamma)$  is much narrower than  $P(\alpha)$  its shape affects only slightly the one of  $G(\theta)$  but mainly induces an increase in the mean value  $\bar{\theta}$  compared to the nominal value  $\theta_0$ . Note that as  $\gamma$  is negative and due to the sign in Eq.20, gravity increases  $|\theta|$  for  $\theta_0 > 0$  but decreases  $|\theta|$  for  $\theta_0 < 0$ . In Fig.12, the angular resolution function  $G(\theta)$  is plotted for  $\theta_0 = 1^\circ$  for the different time-of-flight channels and the three typical configurations of the reflectometer.

## V. RESOLUTION OF TRANSFER VECTOR

The physical parameter related to structural informations on the measured samples is the transfer vector  $q$  (the conjugate variable of distance) that is defined as

$$q = 4\pi \sin(\theta)/\lambda \quad (22)$$

However, the only directly adjustable parameters of the spectrometer are  $\theta$  and  $\lambda$ , both being distributed around  $\theta_0$  and  $\lambda_0$ . For a given time-of-flight channel, the resolution function  $R(q)$  of the transfer vector should be thus a generalized convolution of the probability densities  $H(\lambda)$  (Fig.8) and  $G(\theta)$  (Fig.12) which corresponding random variables are combined following Eq.22. However due to gravity,  $\theta$  and  $\lambda$  are not strictly independent and “convoluting” directly their densities is not correct even if it is a good approximation (because  $J(\gamma)$  is narrow compared to  $P(\alpha)$  in most cases). As moreover this approximation does not save time, we prefer an exact treatment that will

remain valid even in case the width of  $J$  would become significant (see section IV B).

For the sake of simplicity, let us first deal with the “small angle approximation”  $\sin(\theta) \simeq \theta$ . Then, using Eq.20 the transfer vector rewrites:

$$q = \frac{4\pi\theta}{\lambda} = 4\pi \frac{\theta_0 + \alpha - \gamma}{\lambda} \quad (23)$$

where  $\lambda$  and  $\alpha$  are random variables with densities  $H(\lambda)$  and  $P(\alpha)$ , respectively, whereas  $\gamma = -(c\lambda)^2$ . Let us denote  $M(q)$  the measurement of the physical quantity  $m(q)$ . Quite generally, for one time-of-flight channel at  $q_0 = 4\pi\theta_0/\lambda_0$  one can write

$$M(q_0) = \int d\lambda H(\lambda) \int d\alpha P(\alpha) m\left(4\pi \frac{\theta_0 + \alpha - \gamma}{\lambda}\right) \quad (24)$$

Using  $\alpha = (\lambda q/4\pi) - \theta_0 - (c\lambda)^2$  and  $d\alpha = (\lambda/4\pi) dq$ , one gets:

$$\begin{aligned} M(q_0) &= \int d\lambda H(\lambda) \int dq \frac{\lambda}{4\pi} P\left(\frac{\lambda q}{4\pi} - \theta_0 - (c\lambda)^2\right) m(q) \\ &= \int dq m(q) \int d\lambda H(\lambda) \frac{\lambda}{4\pi} P\left(\frac{\lambda q}{4\pi} - \theta_0 - (c\lambda)^2\right) \end{aligned} \quad (25)$$

By definition, the last integral is the resolution function of the transfer vector  $q$ :

$$R(q) = \int d\lambda H(\lambda) \frac{\lambda}{4\pi} P\left(\frac{\lambda q}{4\pi} - \theta_0 - (c\lambda)^2\right) \quad (26)$$

The same procedure can be used for the exact expression  $q = 4\pi \sin(\theta_0 + \alpha - \gamma)/\lambda$  leading to  $\alpha = \sin^{-1}(\lambda q/4\pi) - \theta_0 - (c\lambda)^2$  and  $d\alpha = \lambda dq / \sqrt{(4\pi)^2 - (\lambda q)^2}$ . One obtains:

$$R(q) = \int d\lambda \frac{H(\lambda)\lambda P(\sin^{-1}(\lambda q/4\pi) - \theta_0 - (c\lambda)^2)}{4\pi \sqrt{1 - (\lambda q/4\pi)^2}} \quad (27)$$

Eq.27 can be numerically calculated as is (see python code <https://bitbucket.org/LLBhermes/pytof/>) from Eq.16 (using Eq.15 and 13) and 17. In Fig.13, the whole resolution  $R(q)$  is plotted for the three typical configurations as a function of the time-of-flight channel for  $\theta_0 = 1^\circ$ . Firstly, notice the shift of the mean transfer vector value  $\bar{q} = \int q R(q) dq$  compared to  $q_0$ . This shift results from the wavelength distribution of the incident beam (Fig.9) and from gravity (Fig.11). Both effects contribute to the same result for  $\theta_0 > 0$  but oppose if  $\theta_0 < 0$ . To properly account for this effect, the simplest and more accurate way is to compute the exact resolution function. Secondly, notice that the profile of the exact resolution function differs from its gaussian approximation (see Fig.14). In any case, the exact resolution function has a compact support (i.e.  $R$  is non-zero inside a closed and bounded set of  $q$ -values), unlike gaussian curve that should be numerically cut beyond an arbitrary number of standard deviation. For the configuration allowing a wider resolution, the differences

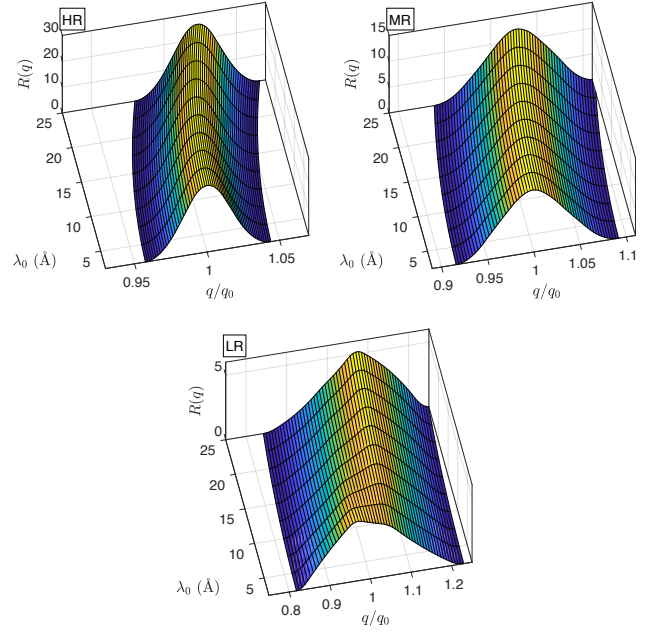


FIG. 13: Total resolution  $R(q)$  of transfer vector  $q$  vs.  $q/q_0$  (x-axis, where  $q_0 = 4\pi \sin(\theta_0)/\lambda_0$ ,  $\theta_0 = 1^\circ$  is the nominal angle) and vs. time-of-flight channel centered on the median wavelength  $\lambda_0$  (y-axis), for the configurations of Table I.

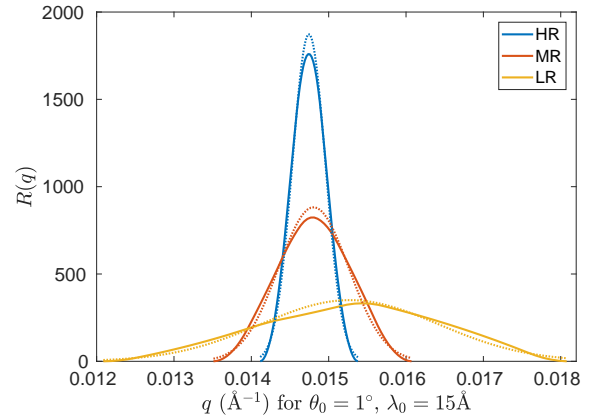


FIG. 14: Exact resolution  $R(q)$  (full line) vs. transfer vector  $q$  for  $\theta_0 = 1^\circ$  and  $\lambda_0 = 15\text{\AA}$  (crosssection of 3D plot of Fig.13), for the configurations of Table I. Dotted lines are gaussian curves of same mean and standard deviation.

between exact resolution and gaussian approximation are much more important and even the modal-values differ. All these differences cannot reasonably be taken into account summarizing the resolution with a simple standard deviation.

## VI. APPLICATION

Let us consider the measurement  $M_i$  (performed with statistical errors bars  $\sigma_i$  with  $i \in \{1, 2, \dots, N\}$ ) of the reflectivity of a sample over  $N$  time-of-flight channels. We denote  $m(q, \mathbf{p})$  the theoretical reflectivity that depends on  $n$  physical parameters that make the coordinates of the vector  $\mathbf{p}$ . For a time-of-flight channel at  $q_i$  of resolution function  $R_i$ , the expected theoretical measurement  $M_{th,i}$  is :

$$M_{th,i}(\mathbf{p}) = \int m(q, \mathbf{p}) R_i(q) dq \quad (28)$$

Let us define the relative distance  $\chi^2$  per channel between  $M$  and  $M_{th}$  as

$$\chi^2(\mathbf{p}) = \frac{1}{N} \sum_{i=1}^N \left( \frac{M_i - M_{th,i}(\mathbf{p})}{\sigma_i} \right)^2 \quad (29)$$

The parameter-vector  $\mathbf{p}$  can be experimentally determined by minimizing  $\chi^2$  following a standard numerical optimization procedure (curve fitting). The correctness of the resolution function can thus be evaluated: 1) from the correctness of the so determined parameters values; and 2) from the correctness of the final matching between  $M$  and  $M_{th}$  (low value for  $\chi^2$  and no correlation in the residual  $(M - M_{th})/\sigma$ ).

For such evaluation, sample-candidate should display a strong variation of reflectivity in the accessible  $q$ -range, in order to maximize the effect of convolution by the resolution function (Eq. 28), with a minimum number of unknown parameters (coordinates of  $\mathbf{p}$ ). From this point of view, the reflectivity near the total reflexion plateau of the interface between air and a smooth and pur solid is likely the most adequate. We have choosen an amorphous silica block with a polished surface, which reflectivity writes :

$$m(q) = \left( \frac{q - \sqrt{q^2 - q_c^2}}{q + \sqrt{q^2 - q_c^2}} \right)^2 \times e^{-h^2 q \sqrt{q^2 - q_c^2}} \quad (30)$$

The first term of this product is the Fresnel's reflectivity of a perfectly flat surface, where  $q_c = (16\pi\rho)^{1/2}$  is the edge of the total reflectivity plateau and  $\rho$  the scattering length density of amorphous silica. Whereas the second term accounts for the surface roughness of characteristic height  $h$ . Measurements were done in the three configurations of Table I for  $\theta_0 = 1^\circ$ . Results and data fitting are plotted in Fig.15. For the three configurations, the value determined for  $q_c$  are in very good agreement and also fully consistent with the density of amorphous silica (here  $\bar{q}_c = 1.307 \times 10^{-2} \text{\AA}^{-1}$  leads to the density  $d = 2.15 \text{ g/cm}^3$  for amorphous silica). Also, the values for  $\chi^2$  at the optimum are very small. The increase of  $\chi^2$  with the broadening of resolution is simply due to the gain of flux resulting in smaller statistical error bars  $\sigma_i$  in Eq.29.

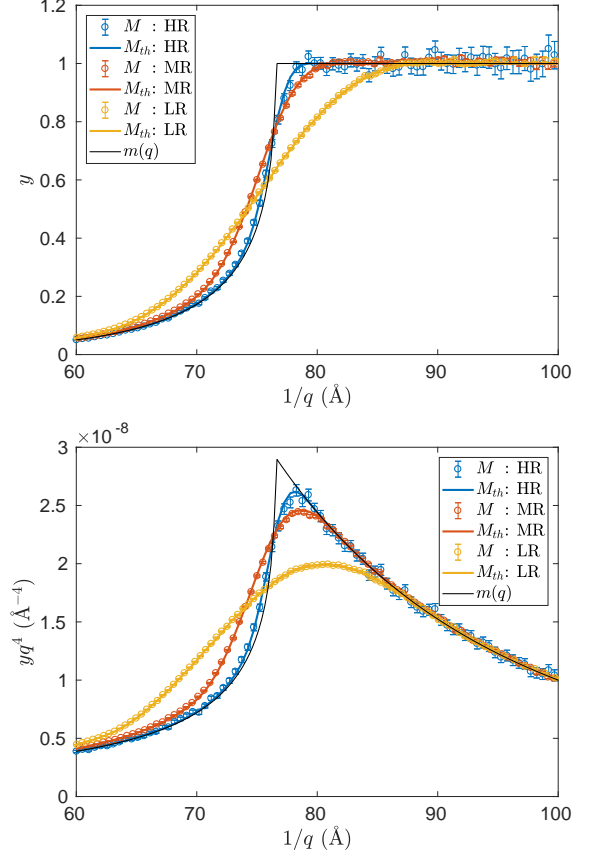


FIG. 15: Reflectivity for an amorphous silica block in the region of the edge of the total reflection. Top: measurement  $M$ , best fit  $M_{th}$  (Eq. 28) and model  $m(q)$  (Eq. 30) vs.  $1/q$  (because channels are almost regularly spaced in wavelength). Bottom: same data with  $y$ -coordinates multiplied by  $q^4$ . For these best fits  $q_c = 1.306, 1.314, 1.300 \times 10^{-2} \text{\AA}^{-1}$  and  $\chi^2 = 0.59, 1.8$  and  $2.4$  for the high-resolution (HR), medium-resolution (MR) and low-resolution (LR), respectively.

The use of the exact resolution function as plotted in Fig.13, should appear unnecessarily tricky compared to the use of a gaussian curve of same average and standard deviation. This is not the case for two reasons: 1) the calculation of the full resolution function is anyway needed to determine the average and standard deviation value; 2) once that is achieved, convolution by the full resolution or its gaussian approximation requires the same computing power. Also, convolution by the full resolution function will always produces better results in particular at low resolution. Best fits obtained using the full resolution or its gaussian approximation (computed over a support-half-width equal to 3 times the standard deviation) are compared in Fig.16-top for the low resolution configuration of Table I. Differences are subtle but are emphasized by plotting the residual  $(M - M_{th})/\sigma$  (Fig.16-bottom) that clearly shows correlations in the case of the gaussian approximation.

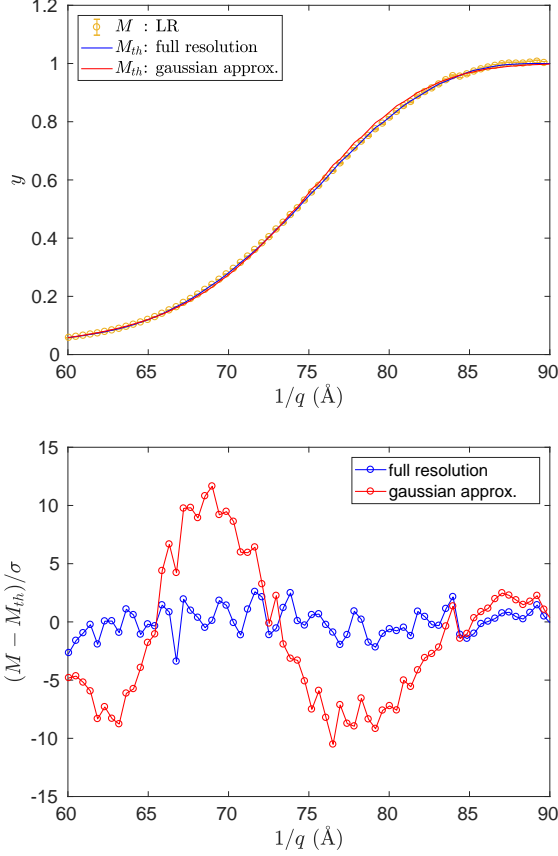


FIG. 16: Reflectivity for an amorphous silica block in the region of the edge of the total reflection plateau. Top: measurement  $M$  and best fits  $M_{th}$  using the full-resolution or its gaussian approximation (computed over a support-half-width equal to 3 times the standard deviation). Bottom: residual  $(M - M_{th})/\sigma$ .

By definition, using the exact resolution function is more accurate than using its gaussian approximation, but it also saves time. Computation of the exact resolution function is done only once during data reduction. The time spent is negligible compared to the time needed for data fitting that consists in many iterations of convolution of a theoretical model by the resolution. The exact resolution function has a compact support whereas its gaussian approximation has not. Thus for a given high percentile, the gaussian approximation needs a more extended sampling and thus is more time consuming during the data fitting stage than the exact function. This removes a lot of interest in the approximation.

## VII. CONCLUSION

In this paper we present the calculation of the exact and comprehensive resolution function for a time-of-flight neutron reflectometer in a way that accounts for all contributions without any assumption of the gaussian distribution or independence of the corresponding variables. The step-by-step procedure matches with a fully documented Python module(<https://bitbucket.org/LLBhermes/pytof/>) that can be easily used for numerical applications to any specific case, from the computation of the resolution to data-fitting. We have shown that in case the resolution is relaxed, the resulting resolution function departs strongly from a gaussian profile and that using the exact function provides much more accurate results. This point will be highly relevant with the emergence of compact and low-flux neutron sources (see e.g. [8]) which will likely require such relaxed resolutions.

- 
- [1] F. Cousin and A. Chennevière, EPJ Web of Conferences **188**, 04001 (2018), URL <https://doi.org/10.1051/epjconf/201818804001>.
  - [2] A. R. J. Nelson, Journal of Applied Crystallography **46**, 1338 (2013), URL <https://doi.org/10.1107/S0021889813021936>.
  - [3] A. A. van Well, Physica B: Condensed Matter **180-181**, 959 (1992), URL [https://doi.org/10.1016/0921-4526\(92\)90521-S](https://doi.org/10.1016/0921-4526(92)90521-S).
  - [4] E. Fermi, W. J. Sturm, and R. G. Sachs, Phys. Rev. **71**, 589 (1947), URL <https://doi.org/10.1103/PhysRev.71.589>.
  - [5] P. Gutfreund, T. Saerbeck, M. A. Gonzalez, E. Pellegrini, M. Laver, C. Dewhurst, and R. Cubitt, Journal of Applied Crystallography **51**, 606 (2018), URL <https://doi.org/10.1107/S160057671800448X>.
  - [6] I. Bodnarchuk, S. Manoshin, S. Yaradaikin, V. Kazimirov, and V. Bodnarchuk, Nuclear Instr. Meth. Phys. Res. A **631**, 121 (2011), URL <https://doi.org/10.1016/j.nima.2010.12.074>.
  - [7] R. Cubitt, T. Saerbeck, R. A. Campbell, R. Barker, and P. Gutfreund, Journal of Applied Crystallography **48**, 2006 (2015), URL <https://doi.org/10.1107/S1600576715019500>.
  - [8] F. Ott, Technical Report, CEA Paris Saclay (2018), URL <https://hal-cea.archives-ouvertes.fr/cea-01873010>.